



Bessel beam generated LIPSS on NiTi wires

Jan Marx¹ · Evgeny L. Gurevich² · Marvin Schuleit¹ · Cemal Esen¹ · Andreas Ostendorf¹

Received: 30 March 2023 / Accepted: 17 June 2023 / Published online: 28 June 2023
© The Author(s) 2023

Abstract

Ultrashort laser pulses are used to generate Laser-Induced Periodic Surface Structures (LIPSS). To apply LIPSS on small confined areas, the laser source must be focused to a small spot diameter. Contrary to commonly used high numerical aperture objectives, we present a Bessel beam-based approach to produce LIPSS covered lines with a width of 4 to 10 μm . Therefore, an 800 nm Ti:Sa-laser with a pulse duration of 110 fs and a repetition rate of 5000 Hz was used. The setup convinces with an extended depth of focus. Thus, high reproducibility of the process was proven, while no focus control and no specific requirements for the surface quality are needed. The applicability of this method is demonstrated by structuring the shell surface of nickel–titanium wires.

Keywords LIPSS · NiTi wires · Axicon · Bessel beam · Ultrashort pulse laser

1 Introduction

Laser-Induced Periodic Surface Structures (LIPSS) are self-organized patterns appearing on different surfaces exposed to short and ultrashort laser pulses. They were first discovered by Birnbaum in 1965 [1] and can be found on metals, semiconductors, dielectrics [2], and even on 2-D materials [3, 4]. One remarkable feature of these structures is that the period of the LIPSS can be much less than the wavelength of the incident laser light. This makes these structures attractive for micro- and nano-patterning. Conditions for the formation of LIPSS with extreme properties such as best homogeneity [5], minimal period [6], or maximal aspect ratio [7] attract much attention during the recent years.

The physical mechanisms of the LIPSS formation are still debated in the literature [8]. It is still not clear whether this periodic pattern is a result of interference between the incident and the surface-scattered electromagnetic waves [9–11], or it is formed by an instability developed in a thin laser-excited surface layer [12–14]. The period of LIPSS generated by the interference mechanism is comparable to

wavelength of the laser, this structure is referred to low spatial frequency LIPSS (LSFL) [8]. A matter of interest, both practically and theoretically, regarding these structures is the minimum size required to cover an area with homogeneous LIPSS. Li et al. [15] reported arrays of LIPSS-covered holes with approximately 1 μm diameter in zinc sulfide. From the theoretical point of view, the answer shades the light on the role of the boundary effects on the periodic pattern [16]. After the crater is formed by the first laser pulses, the electromagnetic waves of the following pulses scattered by the opposite crater edges can interfere with each other, so that the LIPSS period can become dependent on the spot size. The influence of the boundary conditions plays also an important role on the symmetry of the pattern formation in optical systems [17]. One of the possible practical applications of LIPSS is data storage, hence the reduction of the LIPSS-covered area increases the data density [18]. Another need for LIPSS on small confined lines can be found in the field of black marking [19]. The spatial limitation of LIPSS covered areas can help to create deep black patterns with sharp contours, e.g., for identification and security markings [20] of small components, e.g., for medical products [21].

These problems raise the question of the practical methods for making LIPSS on small confined areas: single spots or thin lines. Usually, the following methods are applied to keep the spatial extend of the LIPSS covered area low:

✉ Jan Marx
Jan.Marx@rub.de

¹ Applied Laser Technologies, Ruhr University Bochum, Universitätsstr. 150, 44801 Bochum, Germany

² Laser Center (LFM), University of Applied Sciences Münster, Stegerwaldstraße 39, 48565 Steinfurt, Germany

1. LIPSS are generated using high-NA (numerical aperture) objective to achieve nearly diffraction-limited laser spots. Single LIPSS covered craters of approximately 4 μm in diameter and lines of approximately 2 μm can be achieved in this way, see, e.g., [22]. The drawback of the high-NA optics is the short Rayleigh length—it requires very precise positioning of the sample surface with respect to the laser focus [23], so that reproducible results can be achieved only with great efforts on very smooth flat surfaces.
2. LIPSS are generated very close to the threshold of the LIPSS formation, so that only the very tip of the Gaussian beam profile has enough intensity for LIPSS. Lines of several micrometer width can be made in this way, but this is also only possible on smooth and homogeneous surfaces with high pulse-to-pulse stability of the laser. However, the line width varies as the laser parameters approach the threshold causing irregularities in the lines [24].
3. Recently Bessel beams were proved as a practical tool for the generation of small LIPSS craters due to their small focal spot [15]. Another important advantage of Bessel beams is to overcome high demands on the surface homogeneity as well as on the focus control. Diffraction-limited Bessel beams not only have an extended focus with several tenths of mm in depth but also the diameter of the central core of the Bessel beam profile remains unchanged along the optical axis [25]. This is why they are suitable for processing LIPSS on curved areas [26, 27]. The most common method to produce Bessel beams for micro-processing is focussing a Gaussian beam by an axicon [28, 29]. The characteristic radial intensity distribution of Bessel beams is an interference pattern that shows a narrow central core surrounded by higher order maxima rings. The diameter of the central core (at $1/e^2$) only depends on the axicon angle α , the axicon refractive index n and the wavelength λ of the laser and can be calculated by the following equation [30]:

$$d_s = \frac{1.75 \cdot \lambda}{\pi \cdot \sin(\beta)} \quad (1)$$

with β calculated by the following equation:

$$\beta = (90^\circ - \alpha) - \arccos(n \cdot \cos(90^\circ - \alpha)) \quad (2)$$

Due to the needle-like shape of the central core maximum, the Bessel beam is a well-suited tool for micro-processing structures with sharp contours [31]. Axicons were used earlier to demonstrate LIPSS before by Wang et al. [32], but in a different way. Wang et al. observed LIPSS in the ring-shaped craters formed by the diverging annular beam after the axicon focused by a 20 \times microscope

objective. We notice that pseudo-nondiffracting line focus formed by a wedge reflector (referred to as reflective MEMS axicon) can also be used for large-area periodic pattern formation in the plane perpendicular to the line focus orientation [33]. However, from the images reported in [33], one can argue whether the periodic pattern can be assigned to a self-organisation process, such as LIPSS or DLIP (direct laser interference patterning).

In this paper, we use a Bessel beam-based approach for LIPSS generation on small confined curved surfaces without any precise positioning. In contrast to [33], we use a classical transitive axicon lens and demonstrate LIPSS whose period is smaller than the wavelength of the incident light. The generation of LIPSS on rounded surfaces has already been investigated by Kunz et al. [34], who applied LIPSS to multiple, 10 μm thick carbon fibers at one time. Compared to [34], we precisely processed much thicker single wires with a diameter of 250 μm . We generate the periodic structures on nickel titanium (NiTi) wires. Due to its shape memory effect, NiTi is a highly interesting material in actuator technology [35, 36], e.g., for medical products [37]. Thus, further research into the surface functionalization of NiTi components can, therefore, broaden their range of application. One aspect for future research could be to use the shape memory effect to modify the LIPSS period. LIPSS on flat NiTi surfaces were first observed by Nozaki [38]. Here, we use NiTi wires and demonstrate that despite an inhomogeneous cylindrical surface covered with drawing grooves and the absence of any focusing control, narrow lines filled with homogeneous LIPSS can be achieved. For this purpose, it is essential to make sure only the central core, and not the higher order maxima contribute to the process. It is possible to work with the Bessel beam (central core diameter 11.2 μm) over several millimeters working distance without significant intensity deviations or divergence, while a Gaussian beam with the equal diameter would have a calculated Rayleigh length of just 123 μm .

2 Experimental setup

NiTi wires with a diameter of 250 μm (Ingpuls GmbH, 49.8 at % Ni, martensitic at room temperature, straight annealed) were used for the experiments. Before processing, wires were cleaned in an ultrasonic bath using ethanol. Subsequently, the wires were pickled at 60 $^\circ\text{C}$ for 10 min using Titan-Etch (a mixture of sodium fluoride, ammonium persulphate, and distilled water). Following another cleaning step in the ultrasonic bath for 10 min. This ensures the removal of unwanted surface oxides due to prior heat treatments in the wire production and also improves surface quality. Ultimately, wires were heated to 80 $^\circ\text{C}$ on a hotplate and

then cooled down to room temperature. Thus, the material experiences a shape memory transformation cycle. It transforms into austenite without load when heated, remembers its shape, cools down to room temperature, and converts back into martensite without any further change in shape. Resulting in a non-bent wire with a defined material state, which allows better handling when placing them on the sample holder. The surface topography of the pickled wires was characterized by a 3D laser-scanning microscope (Olympus LEXT OLS 5000). The drawing grooves were dominating the surface roughness having a depth of up to 2 μm .

The sample holder is a steel plate with a U-formed groove in it. The wires were placed over the groove and taped to the steel plate at both ends using copper tape, see inset in Fig. 1. The sample holder was mounted to an xyz -stage [M-521.DD for x - and z -axes, M-521.DG for y -axis, Physik Instrument (PI)] to realize the relative movements between the laser beam and the sample. The experimental setup of the process is shown in Fig. 1.

The beam source used was a Ti:Sa laser (Spitfire Ace, Spectra-Physics) emitting at a central wavelength of 800 nm (60 nm bandwidth). The repetition rate of the laser was set to 5 kHz and the power can be adjusted by rotating a lambda-half plate in front of a polarization filter. Beyond the polarization filter and subsequent mirrors, the laser beam was polarized vertically. The average laser power was measured with a powermeter (VEGA, Ophir Photonics) in front of the axicon to determine the pulse energy. The pulse width of the laser was 110 fs, measured with an autocorrelator (APE Mini, Angewandte Physik & Elektronik GmbH)

behind the beam splitter. An axicon (Thorlabs AX255-B) was used to transform the 8.3 mm Gaussian raw beam into a Bessel beam. The axicon angle was 5° , which results in a good compromise between a small spot diameter and a long focal length with low intensity gradient along the optical axis. The diameter of the central core of the Bessel beam can be calculated by Eq. (1) to 11.2 μm ($1/e^2$). The distance between the axicon and the sample was set to 61.5 mm corresponding to the point of highest intensity of the central core of the Bessel beam.

Single lines of LIPSS were processed on the NiTi wires by moving the stage through the focus of the Bessel beam. The lines were written perpendicular to the wire axis with the laser beam polarization oriented as well along as perpendicular to the writing direction. The starting and ending points of the laser beam trajectory were chosen before and after the wire to make sure that the acceleration and deceleration of the stage axis do not influence the process. In this way, the LIPSS cover the top half of the wire, whereas the distance between the axicon and the sample, the incident angle and the laser spot area and ellipticity change. The velocity of the axis was set to 2.75 mm/s. With the given repetition rate, the spatial distance between two consecutive pulses was 0.55 μm , which results in a pulse overlap of 95% (i.e., 20 pulses per spot).

An Argon gas flow was used to avoid oxidation during the laser process. Therefore, a gas nozzle was placed next to the sample with an angle of 40° to the sample holder surface. The gas flow rate was 8 l/min.

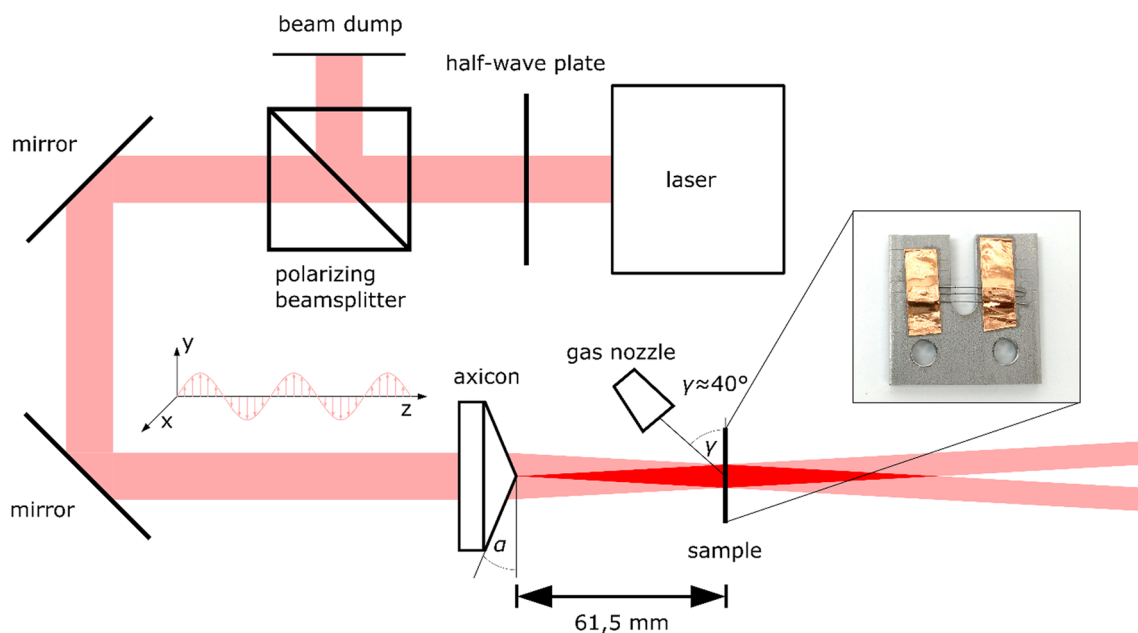


Fig. 1 Axicon-based ($\alpha = 5^\circ$) laser setup and orientation of laser polarization

After the laser process, the samples were cleaned again by the ultrasonic bath to remove possible process debris. A scanning electron microscope (Zeiss EVO MA10) was used to characterize the LIPSS.

3 Results

Two kinds of different orientated LIPSS formation experiments have been carried out. For the first one, the samples were positioned as shown in Fig. 1 to create LIPSS having their ripples aligned perpendicular to the writing direction. Contrary to this, a rotation of the samples by 90° to the fixed polarization of the incident beam leads to LIPSS having their ripples aligned parallel to the writing direction.

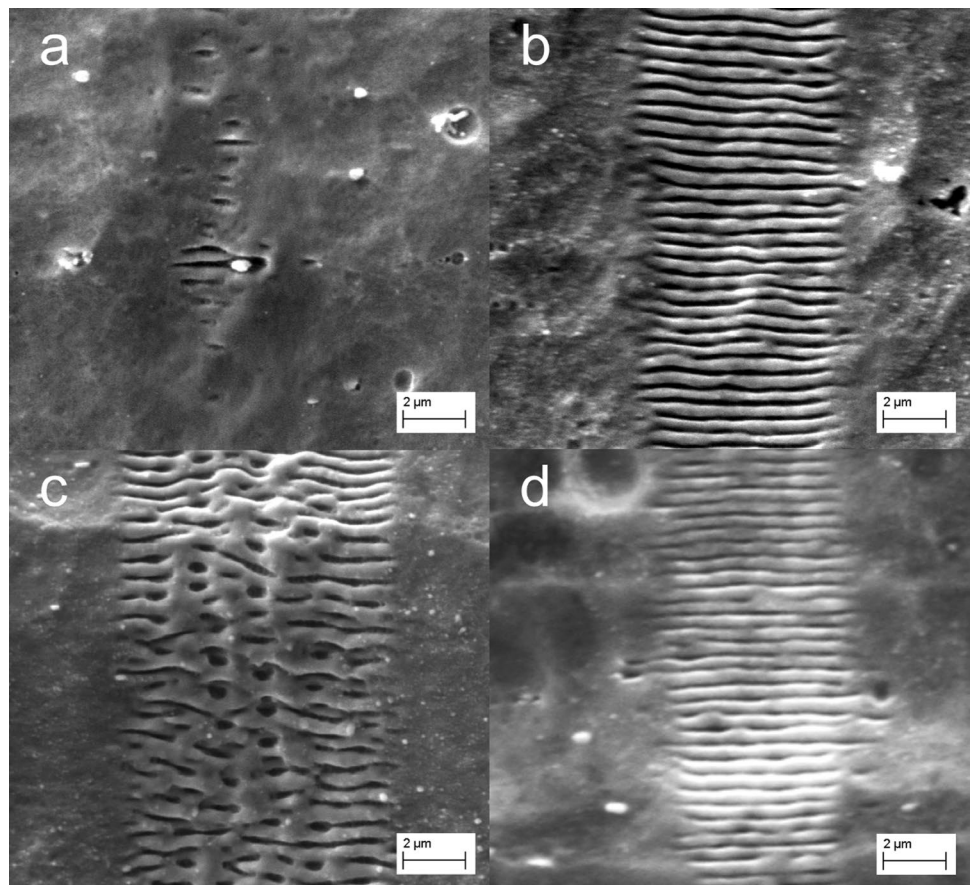
3.1 LIPSS perpendicular to the writing direction

When the writing direction is set parallel to the polarization of the laser beam, the grooves of the LIPSS are aligned perpendicular to the writing direction. Thus, a high number of short grooves was produced by this technique. The experiments were used to determine the period of the LIPSS as well as the width of the processed

lines. Therefore, the pulse energy of the laser was varied between 8 and 100 μJ in steps of 4 μJ . Each experiment was performed on three different samples to prove reproducibility. The measurements of line width and LIPSS period were carried out with the scanning electron microscope (SEM) at the center of the wires, where the optical axis was aligned perpendicular to the surface during the process. Due to the limited resolution of the SEM as well as surface irregularities on the NiTi-wires (e.g., grooves from the wire drawing process), the measurement of the LIPSS period would have been too imprecise. Thus, the length of ten periods was measured and calculated down to a single period.

The results of the experiments can be classified into three different micro structuring regimes. Figure 2 shows a selection of typical surface structures for the different regimes. Up to a pulse energy of 28 μJ , no ablation or LIPSS formation was detected. Just a little darkening of the processed area was observed. The first microstructure regime was in the range between 32 and 36 μJ pulse energy. The processed samples show no homogenous LIPSS pattern, but single patches where LIPSS formation took place (see Fig. 2a). It is suspected that the LIPSS formation started at these patches due to surface irregularities, but the number of pulses in

Fig. 2 Typical results for different pulse energy regimes: **a** LIPSS patches (36 μJ), **b** Homogeneous LIPSS (56 μJ), **c** LIPSS with irregularities (88 μJ). Images **a–c** were taken at the center of the wire, where the incident angle of the laser beam was 0° . **d** Homogeneous LIPSS (56 μJ) at the side away from the center of the wire, where the incident laser angle was 45°



combination with the utilized pulse energy was not sufficient for the LIPSS to expand over the whole focus area.

The second process regime was between 40 and 76 μJ pulse energy, where homogeneous lines of LIPSS were generated (see Fig. 2b). In this process window, the period of the LIPSS was almost constant for the different pulse energies and it was determined to be 517 nm with a standard deviation of 56 nm. Results are similar to the periods measured in [38] and [39] on flat NiTi surfaces with comparable laser central wavelengths. The homogeneity of the LIPSS was disturbed for samples processed with pulse energy of 80 μJ and above in the third pulse energy regime. While the LIPSS are still homogeneous close to the edge of the processed area, the structured lines show lots of irregularities at the center of the line, such as interrupted grooves, bulging material, and arrays of round indentations (see Fig. 2c). The observed material behaviour might be attributed to a change in LIPSS formation orientation caused by the higher fluence in the center of the beam profile. Such fluence-dependent orientation of LIPSS formation has already been observed for other materials [40–42].

With respect to the measured width of the processed lines (shown in Fig. 3), an influence of the interfering pattern surrounding the central core of the Bessel beam itself can be excluded, since the width of all processed lines is smaller than the diameter of the central spot of the Bessel beam. Thus, the intensity of the higher order ring beams around the central core of the Bessel beam did not carry enough energy to form LIPSS on the sample surface. This can also be proven by a theoretical consideration: the spatial intensity distribution of a Bessel beam behind an axicon is given by the following equation [43, 44]:

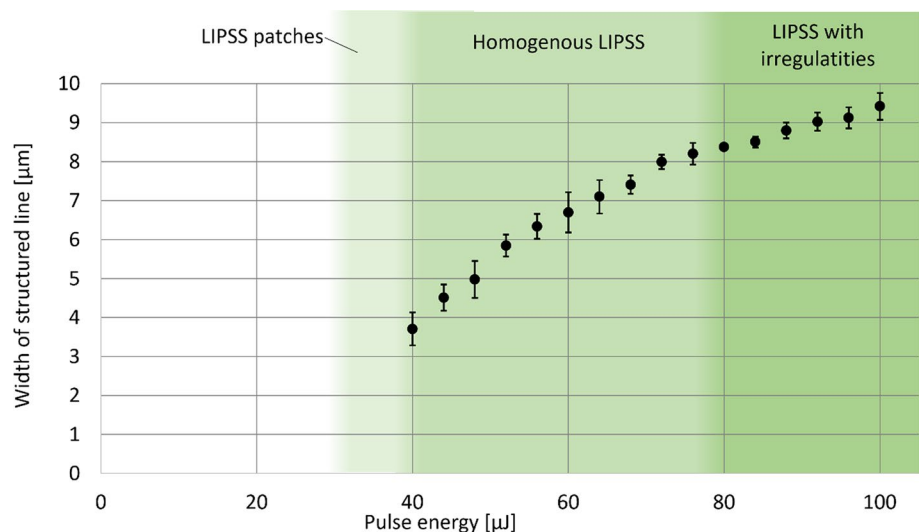
$$I(r, z) = \frac{4\pi^2}{\lambda} \cdot \tan^2(\alpha) \cdot (n - 1)^2 \cdot z \cdot I_0 \cdot \exp\left(-2\left((n - 1) \cdot z \cdot \frac{\tan(\alpha)}{D_0}\right)^2\right) \cdot J_0^2\left(\frac{2\pi}{\lambda} \cdot (n - 1) \cdot r \cdot \tan(\alpha)\right) \tag{3}$$

where r and z are the radial and axial coordinates, respectively. D_0 is the raw beam diameter and I_0 is the on-axis intensity. J_0 is the zero order Bessel function. If Eq. 3 is evaluated at the processing point, it results in a peak intensity ratio between the first ring and central core of 0.16. Due to the linear correlation between pulse energy and peak intensity, the intensity in the first ring around the central core of the Bessel beam is—even for the maximum pulse energy experiments (100 μJ)—below the observed threshold of 32 μJ for LIPSS formation.

The relation of the width of the patterned line versus the applied pulse energy shows an increasing, but degressive trend. This relation can also be attributed to the peaked intensity profile of the central core of the Bessel beam given by Eq. 3. The intensity distribution of the Bessel beam described by Eq. 3 helps to compare the experiments with literature. An evaluation of the equation at the working distance shows, that the central core of the Bessel beam carries only approximately 32% of the energy, the rest is spread to the higher order maxima rings. Thus, only this fraction of the pulse energy E_p must be used to calculate the fluence with the following equation:

$$F_{Bessel,Core} = \frac{2 \cdot 32\% \cdot E_p}{\pi \cdot d_s^2 / 4} \tag{4}$$

Fig. 3 Width of the processed area over the pulse energy and different pulse energy regimes. The different colored areas show the pulse energy regimes, where LIPSS patches, homogeneous LIPSS, or LIPSS with irregularities were detected, respectively



Using Eq. 4, it can be calculated, that, e.g., for the minimum applied pulse energy of $40 \mu\text{J}$ for homogeneous LIPSS generation, the theoretical fluence of the central core of the Bessel beam $F_{\text{Bessel,Core}}$ is 26 J/cm^2 and it is by far higher than the fluence in comparable experiments with Gaussian beams from literature [2]. However, the propagation of ultrashort pulses through an axicon lens is a complex topic, that is in the scope of research for a long time. Some models and simulation have been implemented to understand the mechanisms of ultrashort pulsed Bessel beams [44, 45], but there is still no work that takes into account all effects that occur at once. Thus, it cannot be excluded that the theoretically calculated fluence differs from the actual applied fluence in the experiments. At least, the experimental results confirm, that the polarization does not change by propagating through an axicon, since the ripples are aligned vertically to the polarization direction, as it is known for LSFL structures on metals [2].

To prove the applicability of Bessel beams to uniformly cover the rounded shell surface of the wire, additional investigations were made away from the center of the wire. Figure 2d shows the same LIPSS line as Fig. 2b (processed with $56 \mu\text{J}$ pulse energy), but at the point, where the angle between the surface and the laser beam was 45° . The topography of the LIPSS is similar at both investigated points. The LIPSS period at the incident laser angle of 45° was 480 nm , which is 7% lower compared to vertically incident laser radiation. A reduction in LIPSS period at higher incident laser angles has already been reported for other beam shapes in prior work [24].

3.2 LIPSS parallel to the writing direction

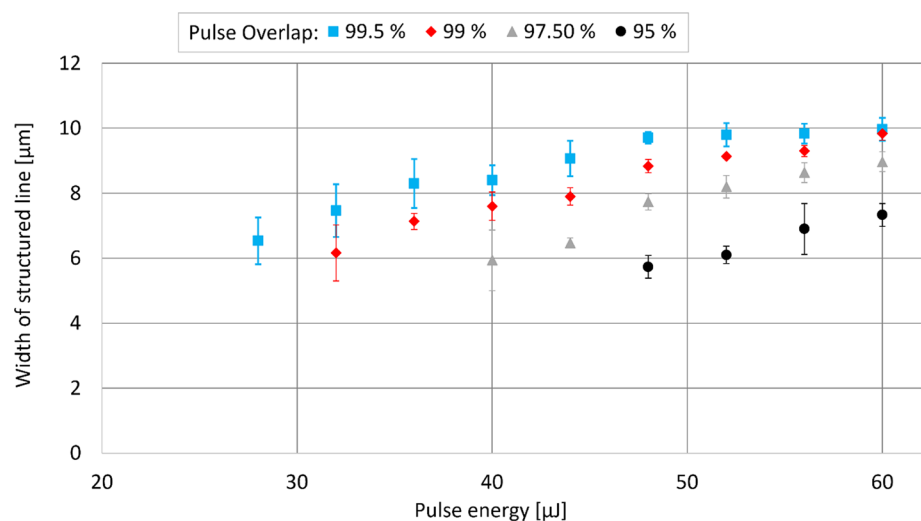
In a second set of experiments, the sample orientation (and with it the LIPSS orientation) was rotated by 90° . Thus, the grooves of the LIPSS were orientated parallel to the

writing direction. The change of the LIPSS formation direction allows to observe whether there are bounding effects determining a smallest possible number of ripples next to each other. The pulse energy was varied in the range between $20 \mu\text{J}$ and $60 \mu\text{J}$ in steps of $4 \mu\text{J}$. The experiments were carried out at a pulse overlap of 95% (20 pulses per spot), 97.5% (40 pulses per spot), 99% (100 pulses per spot), and 99.5% (200 pulses per spot), respectively. Higher pulse overlap was realized by reducing the velocity of the stage axis. The higher pulse overlap should give the LIPSS the chance to expand over large distances instead of creating LIPSS patches as it was observed before. Again, a LIPSS line of each set of parameters was applied to three different samples.

The width of the processed lines was measured and averaged for all samples with a continuous LIPSS covered process zone. The corresponding diagram (Fig. 4) shows some deviations compared to the experiments of the previous section for the pulse overlap of 95%. The threshold for homogeneous LIPSS formation is slightly higher for the LIPSS aligned parallel to the writing direction ($48 \mu\text{J}$ compared to $40 \mu\text{J}$). One possible explanation for the different minimum pulse energy for LIPSS formation is the dependency of the absorption coefficient from polarization direction and the angle between the incident beam and the surface. Although the measurements were made at the center of the wire, the beam is not always aligned normally to the surface because of the drawing grooves covering the surface. Since the drawing grooves are all aligned parallel to the wire axis, the rounded surface of the drawing grooves affect the absorption of both polarization directions to different degrees.

Nevertheless, LIPSS could be generated even with lower pulse energies by reducing the velocity of the stage axis, and thus increasing the pulse overlap. Homogeneous LIPSS have been generated with a pulse energy of $40 \mu\text{J}$ by setting the pulse overlap to 97.5%. With a pulse overlap of 99.5%,

Fig. 4 Width of LIPSS Structures orientated parallel to the writing direction measured in the middle of the lines



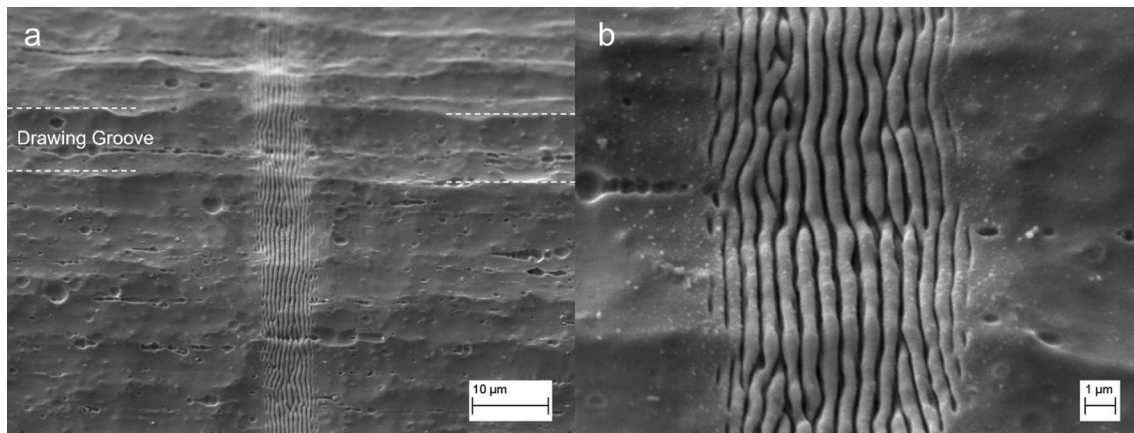


Fig. 5 SEM images of LIPSS aligned parallel to the writing direction processed with 32 μJ pulse energy and 99.5% pulse overlap at different magnifications

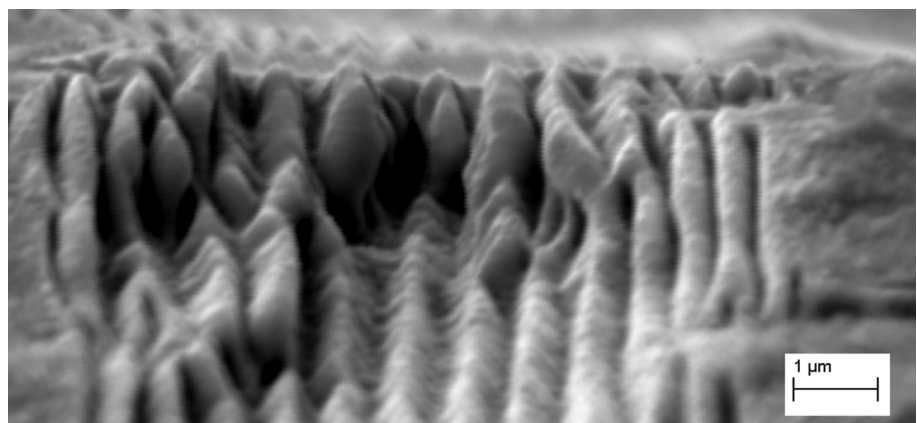
the minimum pulse energy for the generation of homogeneous LIPSS could be reduced to 28 μJ . SEM images of the results are shown in Fig. 5. It can be seen from Fig. 5a, that even with 32 μJ pulse energy, the LIPSS continuously cover the rounded surface of the wire as well as the drawing grooves of the wire. Most of the ripples of the LIPSS extend over several tens of μm . The high pulse overlap allows the LIPSS—once started at irregularities on the wire surface—to extend continuously along the writing path.

With respect to the minimum width of the LIPSS covered lines, Fig. 4 shows some interesting results. Regardless of pulse overlap, the minimum width of homogeneously structured lines is around 6 μm . The measurements were carried out in the middle of the sample, where the beam was perpendicular to the surface. The minimum width of the lines is equivalent to a minimum number of ripples of approximately 10. Regarding to the results the question arises whether there is a minimum number of ripples that can be set next to each other. The results are an indication that the width of the lines cannot be reduced below a minimum. However, proving the

assumption as well as understanding the mechanisms limiting the minimum number of ripples next to each other is beyond the scope this paper, but it is an interesting starting point for future research.

Beside the thin lines at low pulse energies, also the combination of a high pulse overlap and high pulse energies gives some interesting insights into the LIPSS formation. While the laser beam travels over the edges of the drawing grooves of the wire, the height of the LIPSS ripples is in the range of the depth of the drawing grooves. Due to the cylindrical and groove covered surface of the wire, there is a chance to get a sectional view on the ripples without further preparation of the samples by just tilting the sample in the SEM. With a flat surface, however, this view would only be possible after fine cutting and grinding of the processed surface. Figure 6 shows a sample processed at a pulse energy of 60 μJ and with a pulse overlap of 99.5%, where LIPSS ripples with a vertical peak-to-valley distance of 1.5 μm can be observed in

Fig. 6 LIPSS formation on the edge of a drawing groove (pulse energy 60 μJ , pulse overlap 99.5%)



the center of the line. This corresponds to a LIPSS aspect ratio (ratio of the depth to period) > 2 .

4 Conclusion

Within the presented paper, the Bessel beam was successfully proven as a suitable tool for the generation of LIPSS structures in small confined areas. The Bessel beam was used in a pulse energy regime, where only the central core of the Bessel beam contributes to the LIPSS formation. Thus, LIPSS were generated with a minimum spatial extension of 4 to 10 μm . An alignment of the LIPSS parallel to the writing direction resulted in a minimum number of ripples next to each other of approximately 10, with the length of the ripples being several tens of μm . Compared to former research in this field using Gaussian beams and objectives with high numerical aperture, no complex adjustment was required in the presented setup, nor high demands are placed on the evenness of the sample surface. Instead, the long focus of the Bessel beam allows structuring of even complex shaped surfaces with LIPSS, as it was proven on the rounded shell surface of NiTi wires. The LIPSS cover the top half of the wire, which means a difference in working distance of 125 μm . By eliminating the need for any focus control from the process, we believe the presented technique to be an important step towards reliable mass production of LIPSS covered functionalized surfaces.

Acknowledgements We gratefully acknowledge funding by the German Federal Ministry for Economic Affairs and Climate Action under grants 16KN053050 and KK5055205SU1. Furthermore, the authors thank Damian Haske and Tobias Thüsing for their help in preparing the experimental setup and characterization of the samples.

Funding Open Access funding enabled and organized by Projekt DEAL.

Data availability The data that support the findings of this study are available from the corresponding author, JM, upon reasonable request.

Declarations

Conflict of interest The authors declare that they have no conflict of interest.

Open Access This article is licensed under a Creative Commons Attribution 4.0 International License, which permits use, sharing, adaptation, distribution and reproduction in any medium or format, as long as you give appropriate credit to the original author(s) and the source, provide a link to the Creative Commons licence, and indicate if changes were made. The images or other third party material in this article are included in the article's Creative Commons licence, unless indicated otherwise in a credit line to the material. If material is not included in the article's Creative Commons licence and your intended use is not permitted by statutory regulation or exceeds the permitted use, you will need to obtain permission directly from the copyright holder. To view a copy of this licence, visit <http://creativecommons.org/licenses/by/4.0/>.

References

1. M. Birnbaum, J. Appl. Phys. **36**, 3688 (1965). <https://doi.org/10.1063/1.1703071>
2. J. Bonse, J. Krüger, S. Höhm, A. Rosenfeld, J. Laser. Appl. **24**, 42006 (2012). <https://doi.org/10.2351/1.4712658>
3. A. Beltaos, A.G. Kovačević, A. Matković, U. Ralević, S. Savić-Šević, D. Jovanović, B.M. Jelenković, R. Gajić, J. Appl. Phys. **116**, 204306 (2014). <https://doi.org/10.1063/1.4902950>
4. M. Kasischke, S. Maragkaki, S. Volz, A. Ostendorf, E.L. Gurevich, Appl. Surf. Sci. **445**, 197 (2018). <https://doi.org/10.1016/j.apsusc.2018.03.086>
5. I. Gnilitzkiy, T.J.-Y. Derrien, Y. Levy, N.M. Bulgakova, T. Mocek, L. Orazi, Sci. Rep. **7**, 8485 (2017). <https://doi.org/10.1038/s41598-017-08788-z>
6. Y. Borodaenko, S. Syubaev, S. Gurbatov, A. Zhizhchenko, A. Porfirev, S. Khonina, E. Mitsai, A.V. Gerasimenko, A. Shevlyagin, E. Modin, S. Juodkazis, E.L. Gurevich, A.A. Kuchmizhak, A.C.S. Appl. Mater. Interfaces **13**, 54551 (2021). <https://doi.org/10.1021/acsami.1c16249>
7. K. Bronnikov, A. Dostovalov, V. Terentyev, S. Babin, A. Kozlov, E. Pustovalov, E.L. Gurevich, A. Zhizhchenko, A. Kuchmizhak, Appl. Phys. Lett. **119**, 211106 (2021). <https://doi.org/10.1063/5.0075045>
8. J. Bonse, S. Gräf, Laser Photonics Rev. **14**, 2000215 (2020). <https://doi.org/10.1002/lpor.202000215>
9. D.C. Emmony, R.P. Howson, L.J. Willis, Appl. Phys. Lett. **23**, 598 (1973). <https://doi.org/10.1063/1.1654761>
10. J.E. Sipe, J.F. Young, J.S. Preston, H.M. van Driel, Phys. Rev. B **27**, 1141 (1983)
11. J. Bonse, A. Rosenfeld, J. Krüger, J. Appl. Phys. **106**, 104910 (2009). <https://doi.org/10.1063/1.3261734>
12. M. Henyk, N. Vogel, D. Wolframm, A. Tempel, J. Reif, Appl. Phys. A **69**, 355 (1999). <https://doi.org/10.1007/s003390051416>
13. J. Reif, F. Costache, M. Henyk, S.V. Pandelov, Appl. Surf. Sci. **197–198**, 891 (2002). [https://doi.org/10.1016/S0169-4332\(02\)00450-6](https://doi.org/10.1016/S0169-4332(02)00450-6)
14. E.L. Gurevich, Appl. Surf. Sci. **374**, 56 (2016). <https://doi.org/10.1016/j.apsusc.2015.09.091>
15. X. Li, M. Li, H. Liu, Y. Guo, Molecules **26**, 4278 (2021). <https://doi.org/10.3390/molecules26144278>
16. P.N. Terekhin, J. Oltmanns, A. Blumenstein, D.S. Ivanov, F. Kleinwort, M.E. Garcia, B. Rethfeld, J. Ihlemann, P. Simon, Nanophotonics **11**, 359 (2022). <https://doi.org/10.1515/nanoph-2021-0547>
17. F.T. Arecchi, S. Boccaletti, P. Ramazza, Phys. Rep. (1999). [https://doi.org/10.1016/S0370-1573\(99\)00007-1](https://doi.org/10.1016/S0370-1573(99)00007-1)
18. P.I. Trofimov, I.G. Bessonova, P.I. Lazarenko, D.A. Kirilenko, N.A. Bert, S.A. Kozyukhin, I.S. Sinev, A.C.S. Appl. Mater. Interfaces **13**, 32031 (2021). <https://doi.org/10.1021/acsami.1c08468>
19. C. Neugebauer, S. Quaranta, S. Ehrenmann, C. Rest, J. Sadowitz, Proc. SPIE **10906**, Laser-based Micro- and Nanoprocessing XIII (2019) <https://doi.org/10.1117/12.2508408>
20. J. Yang, L. Pabst, W. Perrie, O. Allegre, G. Dearden, S.P. Edwardson, Procedia Eng. **183**, 363 (2017). <https://doi.org/10.1016/j.proeng.2017.04.053>
21. B. Docters, S. Marzenell, M. Kaiser, J. Böhm, H. Breitenborn, R. Groß, S. Rübling, C. Weinert, S. Groß, D. Flamm, B. Block, A. Budnicki, S. Richter, U. Quentert, Proc. SPIE **12411** Frontiers in Ultrafast Optics: Biomedical, Scientific, and Industrial Applications XXIII, (2023) <https://doi.org/10.1117/12.2647720>
22. Y. Borodaenko, S. Syubaev, E. Khairullina, I. Tumkin, S. Gurbatov, A. Mironenko, E. Mitsai, A. Zhizhchenko, E. Modin, E.L.

- Gurevich, A.A. Kuchmizhak, *Adv. Opt. Mater.* **10**, 2201094 (2022). <https://doi.org/10.1002/adom.202201094>
23. A. San-Blas, M. Martinez-Calderon, E. Granados, M. Gómez-Aranzadi, A. Rodríguez, S.M. Olaizola, *Surf. Interfaces* **25**, 101205 (2021). <https://doi.org/10.1016/j.surfin.2021.101205>
 24. S. Schwarz, S. Rung, C. Esen, R. Hellmann, *J. Laser Micro Nanoeng.* (2018). <https://doi.org/10.2961/jlmn.2018.02.0007>
 25. J. Durnin, J.J. Miceli Jr., J.H. Eberly, *Phys. Rev. Lett.* **58**, 1499 (1987)
 26. X. Li, Z. Xu, L. Jiang, Y. Shi, A. Wang, L. Huang, Q. Wei, *Opt. Lett.* **45**, 2989 (2020). <https://doi.org/10.1364/OL.394998>
 27. A. Wang, L. Jiang, X. Li, J. Huang, Z. Xu, Z. Wang, Z. Yao, *Opt. Express* **29**, 5487 (2021). <https://doi.org/10.1364/OE.418663>
 28. M. Kohno, Y. Matsuoka, *JSME Int. J.* **47**, 5 (2004)
 29. M. Duocastella, C.B. Arnold, *Laser Photonics Rev.* **6**, 607 (2012). <https://doi.org/10.1002/lpor.201100031>
 30. Y. Matsuoka, Y. Kizuka, T. Inoue, *Appl. Phys. A* **84**, 423 (2006). <https://doi.org/10.1007/s00339-006-3629-6>
 31. J. Marx, J. Tenkamp, F. Walther, C. Esen, *J. Laser Micro Nanoeng.* **17**, 150 (2022). <https://doi.org/10.2961/jlmn.2022.03.2003>
 32. C. Wang, Z. Luo, J. Duan, L. Jiang, X. Sun, Y. Hu, J. Zhou, Y. Lu, *Laser Phys. Lett.* **12**, 56001 (2015). <https://doi.org/10.1088/1612-2011/12/5/056001>
 33. A. Treffer, S.K. Das, M. Bock, J. Brunne, U. Wallrabe, R. Grunwald, *Proc. SPIE* **8637**, Complex Light and Optical Forces VII, 86370M (2013) <https://doi.org/10.1117/12.2000544>
 34. C. Kunz, T.N. Büttner, B. Naumann, A.V. Boehm, E. Gnecco, J. Bonse, C. Neumann, A. Turchanin, F.A. Müller, S. Gräf, *Carbon* **133**, 176 (2018). <https://doi.org/10.1016/j.carbon.2018.03.035>
 35. L. Fumagalli, F. Butera, A. Coda, *J. Mater. Eng. Perform.* **18**, 691 (2009). <https://doi.org/10.1007/s11665-009-9407-9>
 36. H. Meier, J. Pollmann, A. Czechowicz, *Prod. Eng. Res. Devel.* **7**, 547 (2013). <https://doi.org/10.1007/s11740-013-0481-3>
 37. M. Miro, B. Theren, T. Schmelter, B. Kuhlenkötter, *SMASIS* (2021). <https://doi.org/10.1115/SMASIS2021-67599>
 38. K. Nozaki, T. Shinonaga, N. Ebe, N. Horiuchi, M. Nakamura, Y. Tsutsumi, T. Hanawa, M. Tsukamoto, K. Yamashita, A. Nagai, *Mater. Sci. Eng. C* **57**, 1 (2015). <https://doi.org/10.1016/j.msec.2015.07.028>
 39. H. Wang, F. Pöhl, K. Yan, P. Decker, E.L. Gurevich, A. Ostendorf, *Appl. Surf. Sci.* **471**, 869 (2019). <https://doi.org/10.1016/j.apsusc.2018.12.087>
 40. X. Shi, X. Xu, *Appl. Phys. A* **125**, 9000615 (2019). <https://doi.org/10.1007/s00339-019-2554-4>
 41. S. Gräf, C. Kunz, F.A. Müller, *Materials* **10**, 933 (2017). <https://doi.org/10.3390/ma10080933>
 42. S. Höhm, A. Rosenfeld, J. Krüger, J. Bonse, *J. Appl. Phys.* **112**, 14901 (2012). <https://doi.org/10.1063/1.4730902>
 43. G. Roy, R. Tremblay, *Opt. Commun.* **34**, 2 (1980)
 44. I. Alexeev, K.-H. Leitz, A. Otto, M. Schmidt, *Phys. Proc.* **5**, 533 (2010). <https://doi.org/10.1016/j.phpro.2010.08.177>
 45. S.N. Kurilkina, A.A. Ryzhevich, S.B. Bushuk, S.V. Solonevich, *Quantum Electron.* **38**, 349 (2008). <https://doi.org/10.1070/QE2008v038n04ABEH013717>

Publisher's Note Springer Nature remains neutral with regard to jurisdictional claims in published maps and institutional affiliations.